Improving the Fracture Toughness of Constituent Phases and Nb-Based *In-Situ* Composites by a Computational Alloy Design Approach

KWAI S. CHAN and DAVID L. DAVIDSON

A computational alloy design approach has been used to identify a ductile matrix for Nb-based *in-situ* composites containing Ti, Hf, Cr, Si, and Ge additions. Candidate alloys in the form of cast buttons were fabricated by arc melting. Coupon specimens were prepared and heated treated to vary the microstructure. Backscattered electron (BSE) microscopy, quantitative metallography, energy-dispersive spectroscopy (EDS), and X-ray diffraction (XRD) were utilized to characterize the morphology, volume fraction, composition, and crystallography of individual phases in the microstructure. The fracture toughness of the composites was characterized by three-point bending and compact-tension techniques, while the fracture toughness of individual phases in the *in-situ* composites was determined by an indentation technique. The composition, crystallography, and volume fraction of individual phases were correlated with the fracture-toughness results to assess (1) the role of constituent properties in the overall fracture resistance of the composites and (2) the effectiveness of the computational design approach. The results indicated that the effects of alloy addition and plastic constraint on fracture toughness were reasonably predicted, but the conditions for relaxing plastic constraint to attain higher fracture toughness were not achieved.

I. INTRODUCTION

NB-BASED *in-situ* composites are multiphase alloys that contain an Nb (bcc) solid-solution phase and brittle intermetallic phases such as silicide and Laves phases.[1–12] Depending on the alloy composition, as many as four silicide (Nb_5Si_3, Nb_3Si, Ti_5Si_3, and Ti_3Si) and two Laves phases (C14 and C15 $NbCr_2$) in alloyed forms can exist in the microstructure.[4–6,9–12] $NbCr_2$ is normally C15 at ambient temperature, but transforms to C14 when alloyed with $\simeq$2 at pct Si or greater.[12] The silicide and Laves phases are intended for providing high-temperature creep and oxidation resistance, while the Nb solid solution (Nb_{ss}) is intended to improve the ambient-temperature fracture resistance. Extensive research has demonstrated that alloy additions can impart fracture resistance in the Nb solid-solution, silicide, and Laves phases.[4–11,13–20] The large number of potential alloying elements, however, makes the discovery of beneficial alloy additions a daunting task if undertaken *via* empirical means.

There is considerable interest in developing computational tools for designing materials with a desired composition, microstructure, and performance. For designing against brittle fracture, some investigators[21,22,23] have focused on alloy effects on the unstable stacking energy[24] and the crack-tip dislocation-emission process, while others[17,25–29] have emphasized the influence of alloying additions on the Peierls–Nabarro (P–N) barrier energy[30,31] and the mobility of dislocations moving away from the crack tip. A computational design approach had been developed to identify toughening or embrittling elements on the basis of the P–N barrier energy.[19,25,26] For enhancing fracture toughness and ductility, beneficial alloy additions include Ti, Hf, and Zr, while detrimental alloying elements include Cr, Al, Mo, W, and Re.[26] In this investigation, a computer-assisted alloying approach was used to design Nb-based *in-situ* composites, with the aim of achieving a balance in properties of creep, oxidation, and fracture resistance. In particular, computational models[25,26,32–34] were used to predict alloy compositions based on three considerations: (1) the desired Nb solid-solution alloy, (2) the volume fraction of intermetallics, and (3) the properties of candidate Nb-based *in-situ* composites. The candidate alloys selected by the computational approach were fabricated by arc melting into cast buttons. The microstructure, fracture, and oxidation properties were then characterized. The experimental results were used to assess the predictive capability of the computational design approach and to identify potential areas for model improvement. In this article, the design of the alloy composition, the fabrication, and the characterization of fracture properties of individual constituent phases and the Nb-based *in-situ* composites are reported. The experimental results on the oxidation resistance and oxidation modeling are to be published in a companion article elsewhere,[34] while modeling of the creep resistance of the Nb-based *in-situ* composites was published earlier.[33]

II. DESIGN OF CANDIDATE NB-BASED *IN-SITU* COMPOSITES

The design of candidate materials started with a review of the oxidation data of Nb-based *in-situ* composites in the literature. Additional oxidation data of General Electric (GE) alloys were obtained from the GE Global Research Laboratories (Schenectady, NY).[35] The composition of the

KWAI S. CHAN, Institute Scientist, is with the Southwest Research Institute® (SwRI®), San Antonio, TX 78238. Contact e-mail: kchan@swri.edu DAVID L. DAVIDSON, Consultant, SwRI, is retired.

Manuscript submitted January 16, 2003.

Table I. Compositions of Nb-Based Alloys (in Atomic Percent) and Volume Percents of Silicide, Laves, and Nb_{ss} Constituent Phases Targeted

	Targeted Compositions (At. Pct)						Constituent Phase (Vol. Pct)		
Alloy	Nb	Ti	Hf	Cr	Si	Ge	Silicide	Laves Phase	Nb_{ss}
Nbx	61	28	4	3	1	3	0	0	100
M1	45.5	22.5	4	13	10	5	20	20	60
M2	34.5	22.5	4	16	18	5	30	30	40
AX	40.5	22.5	4	13	15	5	30	20	50
Clp	20.3	10	4	45	20	0.7	0	100	0

Nb matrix in the most-oxidation-resistant *in-situ* composites in the data set were identified. This information was used as input to a composite-design computer code, which is still under development at Southwest Research Institute, to compute the P–N barrier energy,[30,31,36,37] tensile ductility, and fracture toughness for ambient temperature. Based on these results, the compositions of candidate *in-situ* composites in atomic percent were selected and are shown as Nb_{ss} in Table I.

The fracture toughness and the creep strength (at 1200 °C) of *in-situ* composites containing the candidate Nb solid solution were then computed as a function of volume percents of silicides using the methods developed earlier.[32,33] These results were normalized by the target properties ($K_{IC}^* = 25$ MPa$\sqrt{\text{m}}$ at ambient temperature and $\sigma_c^* = 150$ MPa at 1200 °C). Figure 1 indicates that the fracture toughness and creep properties can be achieved when the volume percent of silicides is 32 to 47 pct.

Computation of metal recession using the oxidation model[34] indicated that the oxidation-resistance goal ($X_R^* \leq 25\ \mu$m after 100 hours at 1200 °C, where X_R^* is the maximum recession) could not be achieved if Nb_2O_5 and SiO_2 form on the matrix and silicides, respectively. The oxidation goal could be attained with the formation of a continuous SiO_2 layer, but it would be difficult to achieve because of the low solubility of Si (<2 pct) in the Nb solid solution. Because of this, the strategy used to achieve the oxidation goal was to select alloy compositions that would induce the formation Cr_2O_3 on the Nb solid solution and SiO_2 on the silicides. This approach was selected since the oxidation model of Wang *et al.*[38] suggested that it might be possible to induce the formation of a continuous SiO_2 layer beneath the Cr_2O_3 layer formed on the Nb solid solution, if the silicide and Laves phases are in the form of small disks or spheres.

Based on the previous considerations, we selected the composites AX, M1, and M2 for further studies, whose compositions are shown in Table I along with the compositions of the solid-solution alloy (Nbx) and the Laves alloy (Clp). The Nbx alloy was intended to be the Nb solid-solution phase; unfortunately, small amounts (≈6 to 9 vol pct) of a low-temperature Ge-rich intermetallic phase formed along the grain boundary. In contrast, the composition of the Clp alloy was chosen to give a microstructure of 100 pct C14 Laves phase. In the other alloys, the target for the volume percent of silicide ranged from 20 to 30 pct, and the same ranges were expected

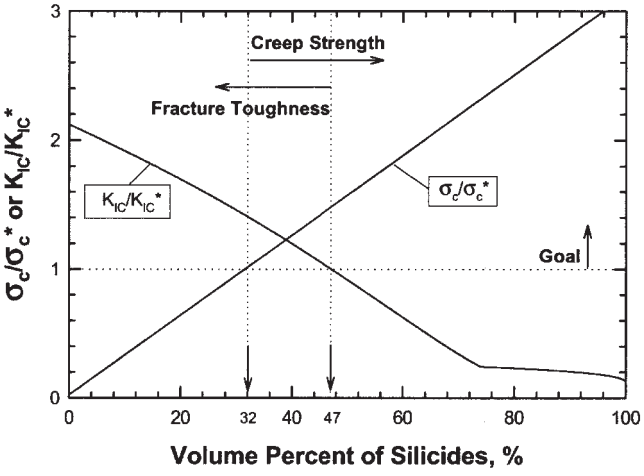

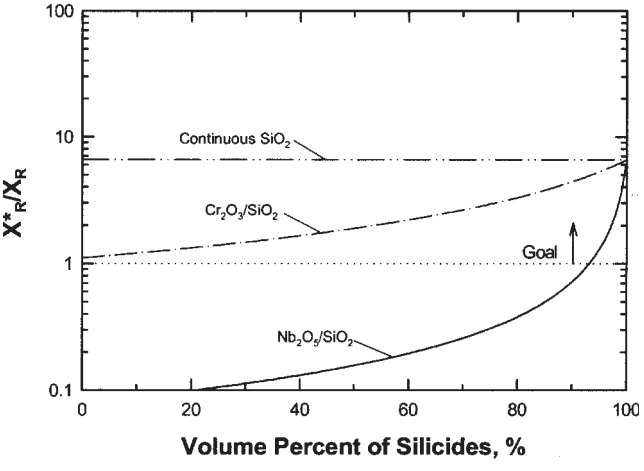

for the C14 Laves phase based on incomplete ternary-phase diagrams available at the time. The total volume percent of silicide and Laves phases was expected to range from 40 to 60 pct, which exceeds the fracture-toughness range shown in Figure 1. Thus, some alloys are shown not to meet the K_C requirement (*e.g.*, AX and M2), but these alloys should manifest higher creep and oxidation resistance compared to other alloys (*e.g.*, M1 and Nbx). These microstructures should provide a sufficiently wide range of properties for a systematic evaluation of the computational design models.

III. EXPERIMENTAL PROCEDURE

A. *Material Fabrication*

One 76-mm-diameter cast button, each, was fabricated for alloys AX, M1, M2, Nbx, and the C14 Laves-phase alloy (Clp). The cast buttons were made by arc melting in a high-purity argon atmosphere at Pittsburgh Materials Technology (PMT). Each of the buttons was remelted 6 times to ensure chemical

Table II. The Actual Chemical Composition and Interstial Contents of Various Nb-Base *In-Situ* Composites

	Compositions (At. Pct)						Interstial Contents (Wt. Ppm)		
Alloy	Nb	Ti	Hf	Cr	Si	Ge	C	N	O
Nbx	62.7	26.6	4.2	2.5	1.0	3.0	<100	62	210
M1	46.3	22.2	4.4	12.3	9.7	5.1	<100	34	320
M2	35.8	22.5	4.0	15.6	17.3	4.8	100	26	220
AX	41.3	22.4	3.9	12.5	14.8	5.1	100	60	220
UES-AX	41.2	23.0	4.7	11.2	15.2	4.7	100	36	280
CNG-1B*	48.7	21.5	2.0	6.7	9.0	4.7	200	44	320

*Also contained 3.5 Pct Fe, 2.6 Pct Al, and 1.3 Pct Sn.

homogeneity. All buttons were cast successfully, except Clp; the C14 Laves-phase alloy exhibited an inhomogeneous microstructure and significant cracking upon cooling.

Besides the PMT-cast buttons, cast bars of alloy AX and an alloy (CNG-1B) that contained Al, Fe, Sn, and B in addition to Ti, Hf, Cr, Si, and Ge, were supplied by the United States Air Force Research Laboratory (AFRL Wright-Patterson Air Force Base, Dayton, OH) through UES (Dayton, OH).[39] The actual chemical compositions of the various alloys are summarized in Table II, which indicates that the actual compositions of the alloys are close to the target, and the interstial contents are low in all alloys.

Coupon specimens were cut from the cast materials and then heat treated. One set of specimens was heat treated at 1350 °C for 100 hours in a flowing argon environment and then furnace cooled (FC), while another set was heat treated at 1350 °C for 24 hours and FC under a similar environment. The UES-AX material was hot-isostatically pressed (hipped) at 1350 °C under a pressure of 207 MPa for 6 hours before it was heat treated (1350 °C/100 hours/FC). The CNG-1B alloy received the same heat treatment (1350 °C/100 hours/FC), but it was subsequently hipped at 1420 °C under 207 MPa pressure for 6 hours and FC.

B. *Characterization of Microstructures*

Backscattered electron (BSE) microscopy was used to characterize the microstructures of various Nb-based *in-situ* composites. Figure 2 shows the microstructure of the various materials heat treated at 1350 °C/100 hours. Because of atomic-number contrast, Nb-based solid solution appeared as the light phase, Nb-rich silicides (Nb_5Si_3 and Nb_3Si) appeared as the medium-dark or gray phase, and the Laves phase (C14) appeared as the dark phase in the BSE images. Ti-rich silicides (Ti_5Si_3 and Ti_3Si) and Hf particles were occasionally detected, and they appeared as one of the light phases in the BSE micrographs.

Using BSE micrographs, quantitative metallography was used to determine the volume fractions of silicides (Nb_5Si_3, Nb_3Si, Ti_5Si_3 and Ti_3Si), Laves phases, and Nb-based solid solution. Since Ti-rich silicides and Hf particles sometimes appeared as a light phase in the BSE images, the volume fraction of Nb solid solution might be overestimated due to the presence of Ti-rich Ti_5Si_3 and Hf particles, but the error was expected to be small because both Ti_5Si_3 and Hf particles were detected only occasionally. Summaries of the chemical compositions and volume fractions of constituent phases (silicides, Laves phase, and Nb solid solution) in the various materials are presented in Tables III and IV, respectively.

The compositions of individual phases in individual Nb-based *in-situ* composites were determined by energy-dispersive spectroscopy (EDS) performed on selected grains. Some of these grains had been indented to measure the fracture toughness using the Vickers indentation technique. Furthermore, the crystal structure of individual phases in the composites was identified by X-ray diffraction (XRD) and by comparing the diffraction peaks against published standards. After fracture testing, the fracture surfaces were characterized by a scanning electron microscope (SEM) operated in the secondary-electron mode.

C. *Fracture-Toughness Testing*

The fracture toughness of individual composites was determined by three-point bending of notched specimens. The specimen dimensions were 40 mm in length, 6 mm in width, and 3 mm in thickness, with a 3-mm notch fabricated by electrodischarge machining (EDM). Fracture-toughness testing was performed at 25 °C using a loading rate of 60 N/s, and the applied load was measured as a function of displacement. The peak load was used to compute the fracture toughness using the analysis described in the ASTM standard.[40] Triplicate specimens were tested for the as-cast alloys, which showed relatively small scatter; consequently, a single test was performed on most of the heat-treated specimens.

Compact-tension specimens with a fatigue precrack were also used to determine the fracture toughness of individual alloys. The specimen dimensions were 20 mm in width, 19 mm in height, and 4.8 mm in thickness. The specimens were fabricated by EDM and contained a notch of 7.14 mm in length. Fatigue cracks were introduced at 25 °C by cyclic loading at an R ratio of 0.1, where R is the ratio of the minimum to maximum load. After precracking, fracture-toughness testing was performed at 25 °C in an SEM equipped with a loading stage.[41] The near-tip region was first photographed at a stress-intensity factor (K) of about 5 $MPa\sqrt{m}$. Subsequently, the K level increased by 1 $MPa\sqrt{m}$, and the near-tip region was photographed again in order to identify the fracture process and follow the crack path. This process was repeated until final fracture of the specimen occurred. Crack extension at each K increment was measured from the near-tip photographs, and the K-resistance curve was obtained by plotting K as a function of crack extension.

In addition, the fracture toughness of the constituent phases in individual alloys was determined at 25 °C by the Vickers indentation technique.[42] A Vickers-hardness indent was made in the phase of interest using a small indentation load. The load was selected such that it was large enough to produce indentation cracks but was sufficiently low that the resulting Vickers indent and cracks resided entirely within the phase of interest. For silicide and Laves phases, fracture toughness was determined using an indention load of 20 or 50 g. At these load levels, indentation cracks were induced in the Nb solid solution only occasionally, and most of the indents produced no cracks at loads as high as 200 g. After indentation, individual indents were photographed in the SEM using the BSE

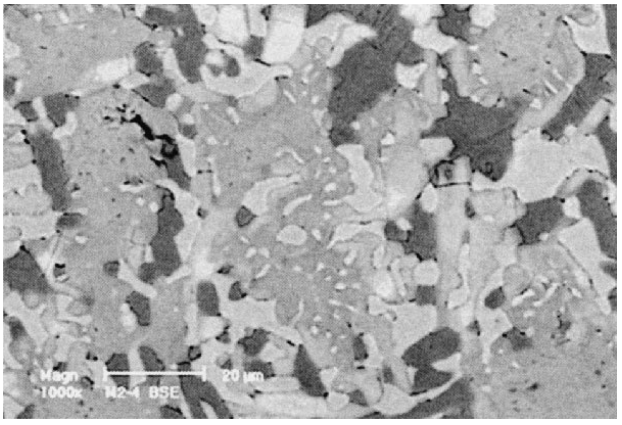

(*a*)

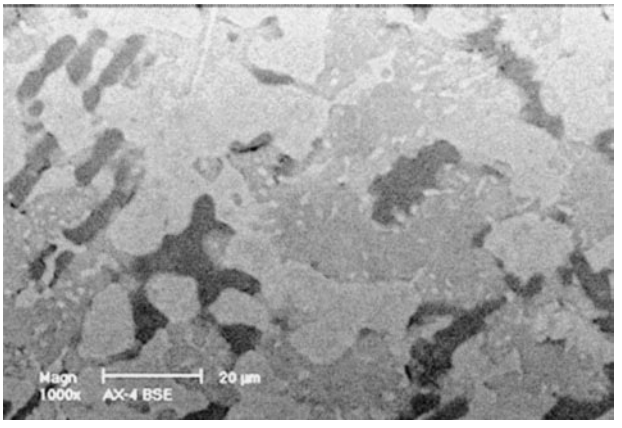

(*b*)

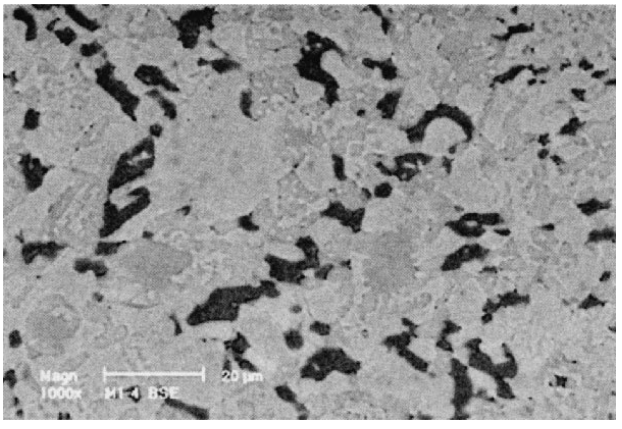

(*c*)

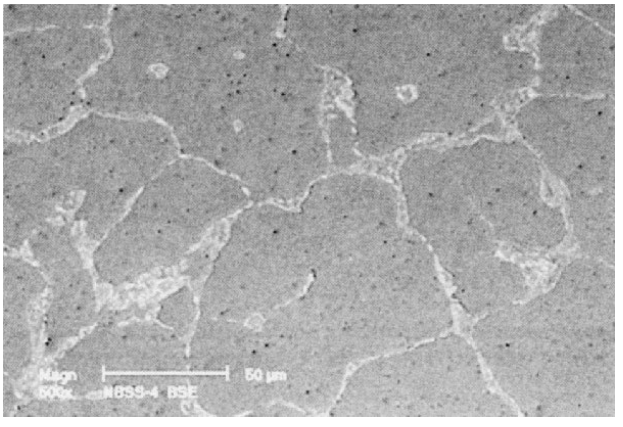

(*d*)

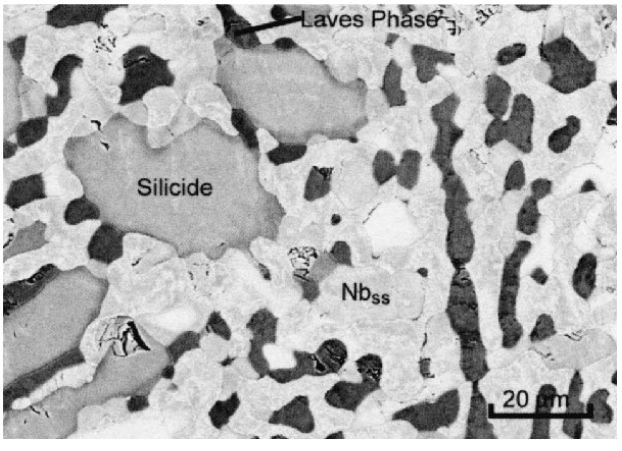

(*e*)

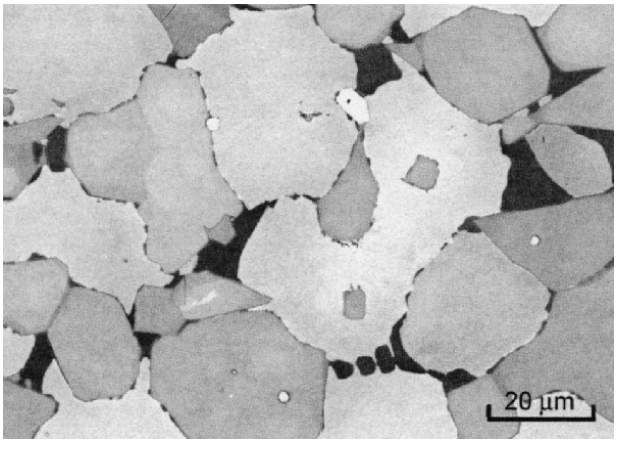

(*f*)

mode. The chemical composition of the indented grain with microcracks was determined by energy-dispersive spectroscopy. The size of the indents and the corresponding crack lengths were then determined from the BSE photographs. These results were then used to obtain the indentation fracture toughness.

According to Anstis *et al.*,[42] the indentation toughness (K_{VC}) can be computed using the expression given by[42]

$$K_{VC} = \phi_V (E/H)^{1/2} P/c^{3/2} \qquad [1]$$

where E is the Young's modulus, H is the hardness in units of MPa, P is the indentation load, c is the crack length measured from the apex of the Vickers indent, and ϕ_V is a load/boundary correction factor. The origin of the load/boundary correction factor was investigated by several investigators.[42,43,44] These investigations indicated that the tensile stress that caused crack initiation and growth in an indentation-toughness test was induced under the indentor during unloading.[42,43,44] The manner by which these tensile stresses were induced was analogous to that at a notch root subjected to

Table III. The Chemical Compositions and Crystal Structures of Constituent Phases in Various Nb-Based *In-Situ* Composites in the As-Cast and Heat-Treated Conditions

Alloy	Heat Treatment	Nb_{ss} Phase (bcc)	Silicide Phase* ($D8_1$)	Laves Phase (C14)	Ge-Rich Phase (Unknown)
M2-1	as-cast	—	Nb-23Ti-3Hf-4Cr-6Ge-28Si	Nb-12Ti-4Hf-52Cr-2Ge-9Si	—
M1-1	as-cast	Nb-20Ti-3Hf-12Cr-4Ge-4Si	Nb-20Ti-4Hf-3Cr-10Ge-25Si	Nb-10Ti-4Hf-49Cr-2Ge-9Si	—
AX-1	as-cast	Nb-24Ti-3Hf-14Cr-2Ge-1Si	Nb-21Ti-3Hf-3Cr-8Ge-27Si	Nb-15Ti-6Hf-49Cr-2Ge-8Si	—
Nbx-1	as-cast	Nb-29Ti-4Hf-3Cr-3Ge-3Si	—	—	Nb-39Ti-6Hf-3Cr-9Ge-6Si
UES-AX	1350 °C/100 h	Nb-26Ti-3Hf-14Cr-3Ge-1Si	Nb-24Ti-4Hf-1Cr-6Ge-29Si	Nb-12Ti-3Hf-54Cr-1Ge-8Si	—
M2-3	1350 °C/100 h	Nb-23Ti-1Hf-10Cr-3Ge-3Si	Nb-19Ti-5Hf-2Cr-7Ge-28Si	Nb-12Ti-4Hf-50Cr-2Ge-8Si	—
M1-3	1350 °C/100 h	Nb-18Ti-1Hf-10Cr-2Ge-3Si	Nb-17Ti-5Hf-3Cr-12Ge-23Si	Nb-10Ti-4Hf-49Cr-2Ge-9Si	—
AX-3	1350 °C/100 h	Nb-20Ti-1Hf-10Cr-3Ge-3Si	Nb-18Ti-5Hf-1Cr-8Ge-28Si	Nb-11Ti-4Hf-48Cr-2Ge-9Si	not determined
Nbx-3	1350 °C/100 h	Nb-24Ti-3Hf-3Cr-4Ge-3Si	—	—	Nb-28Ti-19Hf-0.3Cr-27Ge-10Si
CNG-1B**	1350 °C/100 h	Nb-21Ti-.1Hf-8Cr-0.8Ge-0.8Si-2.6Fe-2Sn-2Al	Nb-19Ti-2.3Hf-1.7Cr-9.5Ge-20Si-2Al-1.8Fe-1Sn	Nb-15Ti-2.8Hf-31Cr-1Ge-8Si-2Al-15Fe-0.1 Sn	—

**Hipped at 1420 °C under 207 MPa pressure for 6 h.
*Also contained small amounts of $(Ti, Nb)_5Si_3$ ($D8_8$ structure) and possibly Nb_3Si (Ti_3P structure).

Table IV. A Summary of the Volume Percents of Intermetallics and Fracture Toughness Results for Nb-Based *In-Situ* Composites Determined by Three-Point Bend and Compact Tension (CT) Techniques

Alloy	Heat Treatment	Vol Pct Nb_{ss}	Vol Pct Silicides	Vol Pct Laves Phase	Vol Pct Ge-Rich Phase	K_C, $MPa\sqrt{m}$ (3-Point Bend)	K_C, $MPa\sqrt{m}$ (CT Tests)
M2-1	as-cast	0	73	27	0	8.4 ± 1.2*	8.8
M1-1	as-cast	64	28	8	0	12.2 ± 0.7*	—
AX-1	as-cast	20	66	14	—	10.3 ± 0.3*	9.9
Nbx-1	as-cast	91	—	—	9	22.1 ± 2.2*	—
UES-AX	1350 °C/100 h	54	32	14	—	10.9 ± 1.4*	11.4
M2-3	1350 °C/100 h	22	53	25	—	7.4	—
M1-3	1350 °C/100 h	54	35	11	—	13.1	—
Nbx-3	1350 °C/100 h	94	—	—	6	24.7	—
AX-3	1350 °C/100 h	39	40	15	6	11.8	—
CNG-1B**	1350 °C/100 h	43.6	50.7	5.7	—	6.3 ± 0.2*	11.0
M2-4	1350 °C/24 h	24.0	48.7	26.5	—	8.7	—
M1-4	1350 °C/24 h	60.2	27.9	10	—	11.5	—
AX-4	1350 °C/24 h	50.6	33.7	14	—	10.1	—
Nbx-4	1350 °C/24 h	83.7	—	—	16.3	27.2	—

**Hipped at 1420 °C under 207 MPa pressure for 6 h.
*Average of three tests.

compression/compression fatigue.[45,46,47] In particular, the tensile stresses induced during unloading depend on the amount of inelastic deformation that occurred at the notch root. Inelastic deformation corresponds to plastic flow for ductile materials,[45] but originates from microcracking for brittle materials.[46,47] In general, Eq. [1] is applied to brittle materials, and the value of ϕ_V was evaluated by fitting Eq. [1] to a set of fracture-toughness data for ceramics.[42] Since the tensile stresses induced during indentation depend on inelastic deformation under the indentor, it was uncertain whether Eq. [1] was applicable to Nb-based *in-situ* composites. Consequently, the fracture-toughness data of three-point bend tests were used to calibrate Eq. [1] to obtain the appropriate value for the load/boundary correction factor (ϕ_V). The ϕ_V value was found to be 0.1168 for Nb-based composites, compared to $\phi_V = 0.016$ for brittle ceramics.[42] Once ϕ_V was determined, Eq. [1] was used to compute the K_{VC} values for individual phases (silicides, Laves phase, and Nb*ss*) in the *in-situ* composites.

IV. RESULTS

A. *Microstructure*

Typical XRD results of the as-cast materials are presented in Figures 3(a) and (b). Individual phases were identified by matching the characteristic XRD peaks against the JCPDF standards.[48] In as-cast M2, the microstructure was comprised of alloyed Nb_5Si_3, Nb_3Si, Ti_5Si_3, and $NbCr_2$; there was little or no Nb solid solution, since the observed XRD peaks did not match those of Nb (Figure 3(a)). In alloys M1 and AX, the microstructure contained Nb solid solution, alloyed silicides (Nb_5Si_3, Nb_3Si, and Ti_5Si_3), and alloyed $NbCr_2$; the results for M1 are shown in Figure 3(b). For alloy Nbx, XRD results showed only the Nb solution phase, but BSE microscopy indicated the presence of a Ge-rich grain-boundary phase that was identified as a low-melting-point metastable intermetallic.[49] The microstructures of the heat-treated

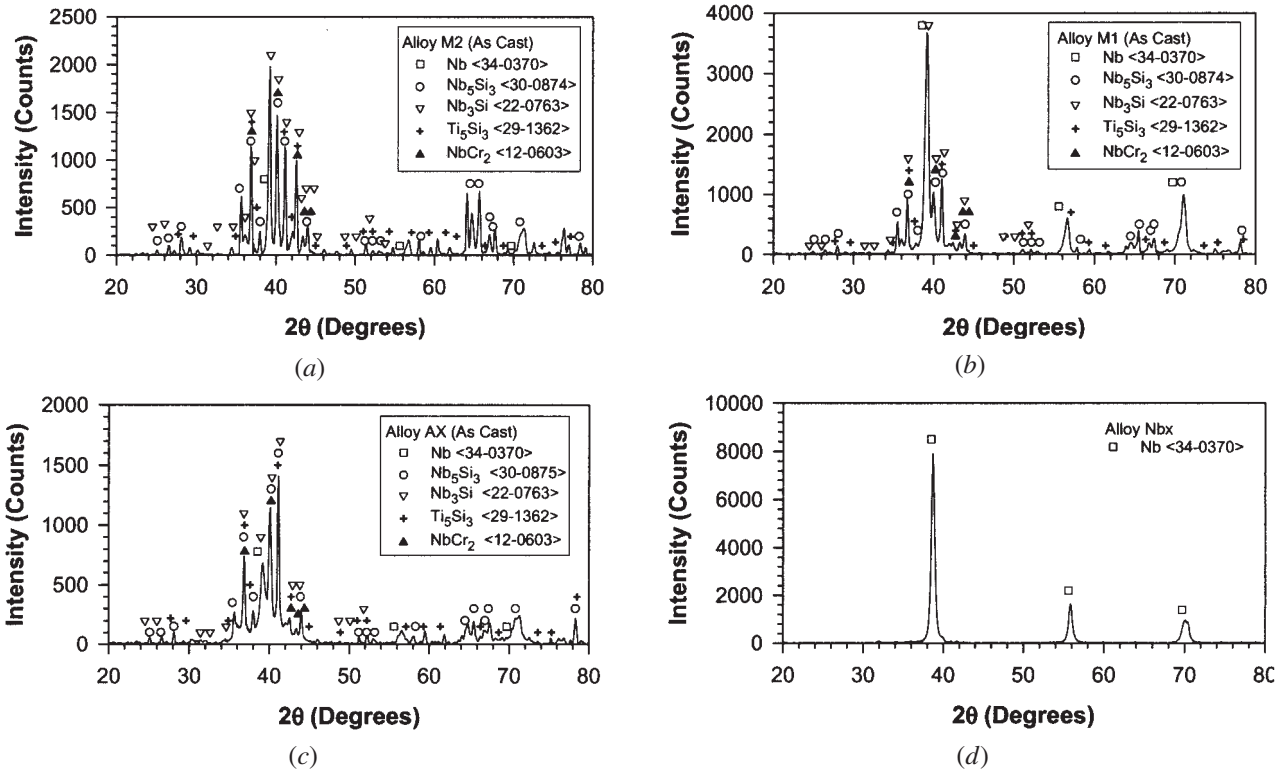

Fig. 3—Typical XRD results of as-cast Nb-based *in-situ* composites: *(a)* M2, *(b)* M1, *(c)* AX, and *(d)* Nbx. The <> shows the JCPDF card number.

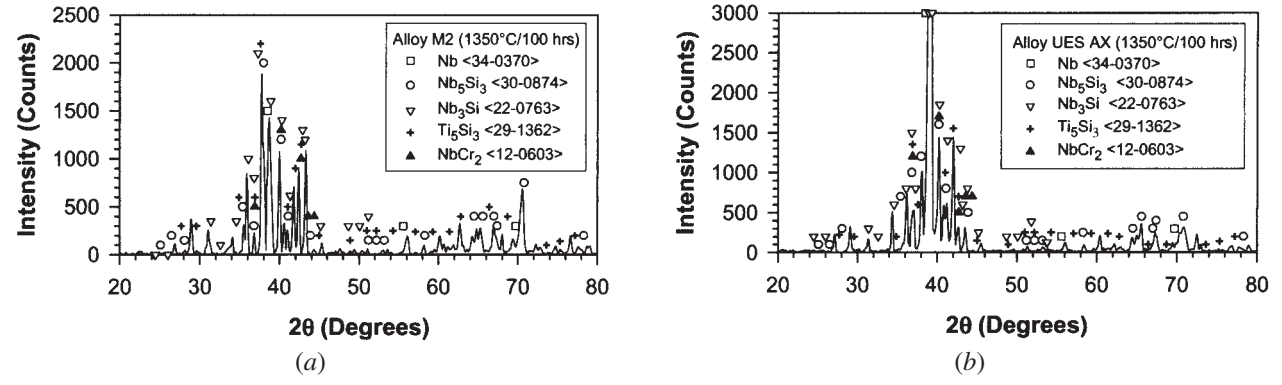

Fig. 4—Typical XRD results of Nb-based *in-situ* composites heat treated at 1350 °C for 100 h: *(a)* M2 and *(b)* UES-AX. The <> shows the JCPDF card number.

materials (1350 °C/100 hours and 1350 °C/24 hours) were comprised of Nb solid solution, alloyed silicides (Nb_5Si_3, Nb_3Si, and Ti_5Si_3), and alloyed $NbCr_2$. Typical results for M2 and UES-AX, which were heat treated at 1350 °C/100 hours, are presented in Figures 4(a) and (b), respectively.

Compositions of alloyed silicide, Laves phase, and Nb_{ss} in Nb-based *in-situ* composites are presented in Figure 5. The crystal structures of alloyed Nb_5Si_3, Nb_3Si, Ti_5Si_3, and $NbCr_2$, which were identified by matching the observed diffraction peaks against the JCPDF and then consulting the corresponding data cards,[48] are $D8_1$, Ti_3P, $D8_8$, and C14, respectively, as summarized in Table III.

The phase diagrams for Nb-based i*n-situ* composites containing three or more alloying elements are generally not available. Fortunately, Bewlay and Jackson[11] and Zhao *et al.*[12] recently published several ternary-phase diagrams for the Nb-Ti-Si, Nb-Cr-Si, and Nb-Ti-Cr systems for selected temperatures in the range of 1000 °C to 1350 °C. Although the temperature was sometimes different, these phase diagrams were used to compare with the experimental data obtained in this study by treating selected elements as equivalent. For examples, Ti and Hf were treated as equivalent and, similarly, Si and Ge were considered equivalent. Figures 6(a) through (c), respectively, show the as-cast alloys in three pseudoternary phase diagrams for 1350 °C: Nb-Ti(+Hf)-Si(+Ge + Cr), Cr-Nb (+Ti + Hf)-Si(+Ge), and Nb-Ti(+Hf)-Cr(+Si + Ge). The phase boundaries shown in Figure 6(a) are for 1350 °C and are taken from Bewlay *et al.*[11] In Figures 6(b) and (c), the phase boundaries are for 1200 °C and both are from Zhao *et al.*[12] The results indicate that the alloys are located

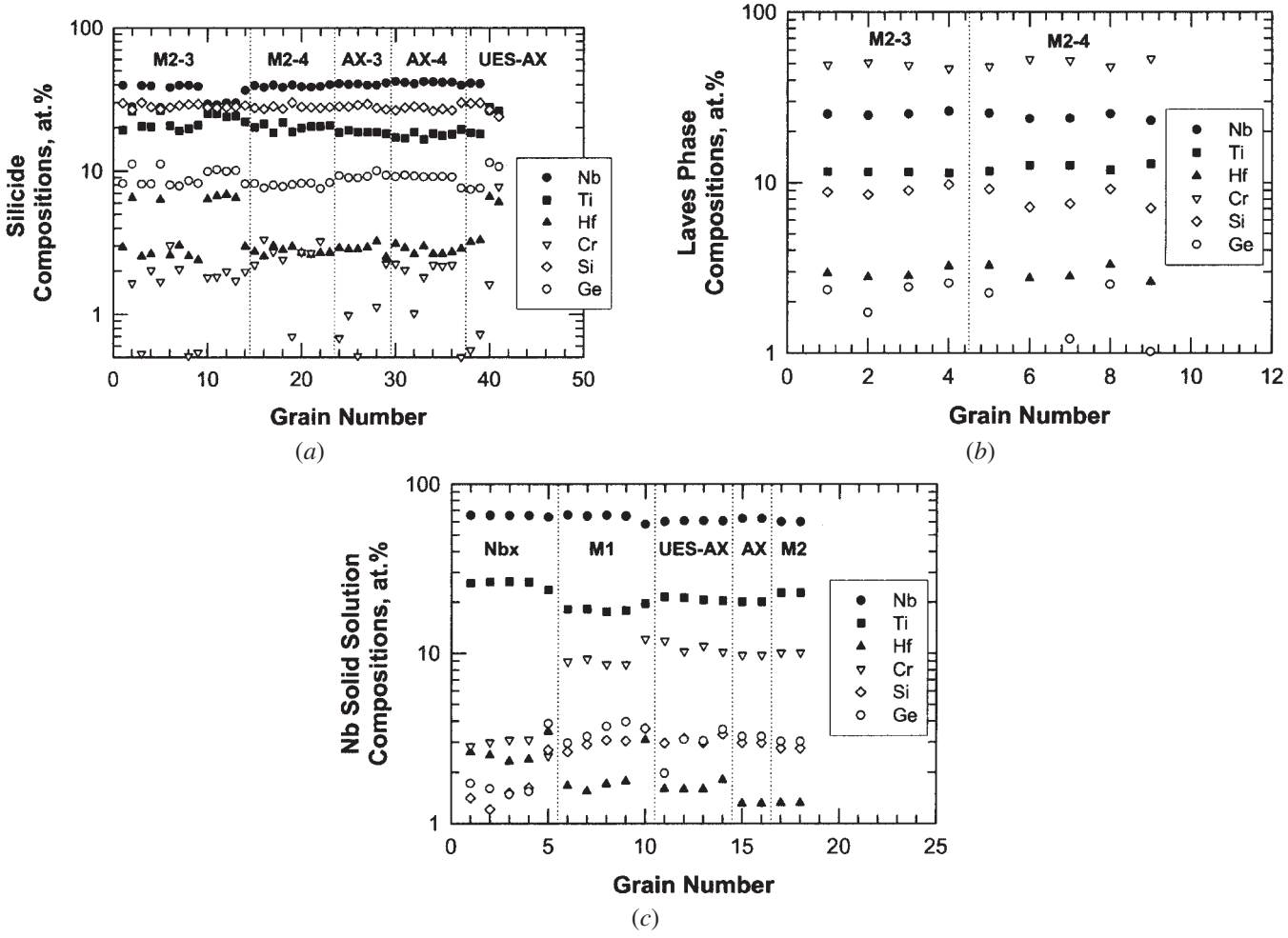

Fig. 5—Typical compositions of constituent phases in Nb-based *in-situ* composites: (*a*) silicide, (*b*) Laves phase, and (*c*) Nb_{ss}. The heat treatment was 1350 °C/100 h for all specimens except M2-4 and AX-4, which were heat treated at 1350 °C/24 h. The grain number was assigned arbitrarily for plotting purposes only.

in a three-phase field containing silicides, Laves phase, and Nb solid solution, with the exception of as-cast M2, which contained silicides and Laves phase only. Another important observation from Figure 6 is that the compositions of the constituent phases are similar in the various *in-situ* composites, the only exception being Nbx, whose Nb solid solution exhibits a lower Cr content (≈3 at. pct Cr) than those in other materials (9 to 14 at. pct Cr). Thus, the main difference among the various composites is in their volume fractions of the constituent phases. The discrepancies observed in the current data and the phase boundaries in Figures 6(b) and (c) are probably due to variants in the temperature of the phase diagram. Unfortunately, ternary-phase diagrams for Cr-Nb-Si and Nb-Ti-Cr at 1350 °C do not appear to be available in the literature.

B. *Fracture Toughness*

The fracture-toughness values of Nb-based *in-situ* composites, determined by three-point bend and compact-tension specimens, are summarized in Table IV. The results are also plotted against the volume percent of intermetallics in Figure 7. In general, K_C decreases with increasing volume percent of silicide and Laves phases in the composite. Heat treatments varied the volume percents of the silicides, but the volume percent of Laves phase remained essentially unchanged before and after heat treatment. Despite these changes, the fracture toughness was not significantly altered by heat treatment, as shown in Figure 7. The fracture toughness of the *in-situ* composites appears to remain constant at approximately 10 $MPa\sqrt{m}$ when the volume percent of silicides and Laves phase exceeded about 50 pct.

Typical indentation cracks in Laves phase, silicide, and Nb solid solution are shown in Figure 8. The indentation toughness of the Laves phase ranged from 2 to 5 $MPa\sqrt{m}$. In contrast, the indentation toughness of the silicide phases ranged from 3 to 12 $MPa\sqrt{m}$. The frequency distribution of K_C for the silicides was measured, and the result is presented in Figure 9. Only some Nb_{ss} grains in AX and UES-AX cracked by indentation, most of the Nb_{ss} grains in M1 did not crack, and none in the Nbx cracked by indentation. Since the Nb solid-solution Nbx did not crack under indentation, only the minimum values of the indentation toughness could be estimated, and they ranged from 22 to 32 $MPa\sqrt{m}$ (Figure 10). The actual toughness of the Nb solid solution in Nbx exceeded these minimum values.

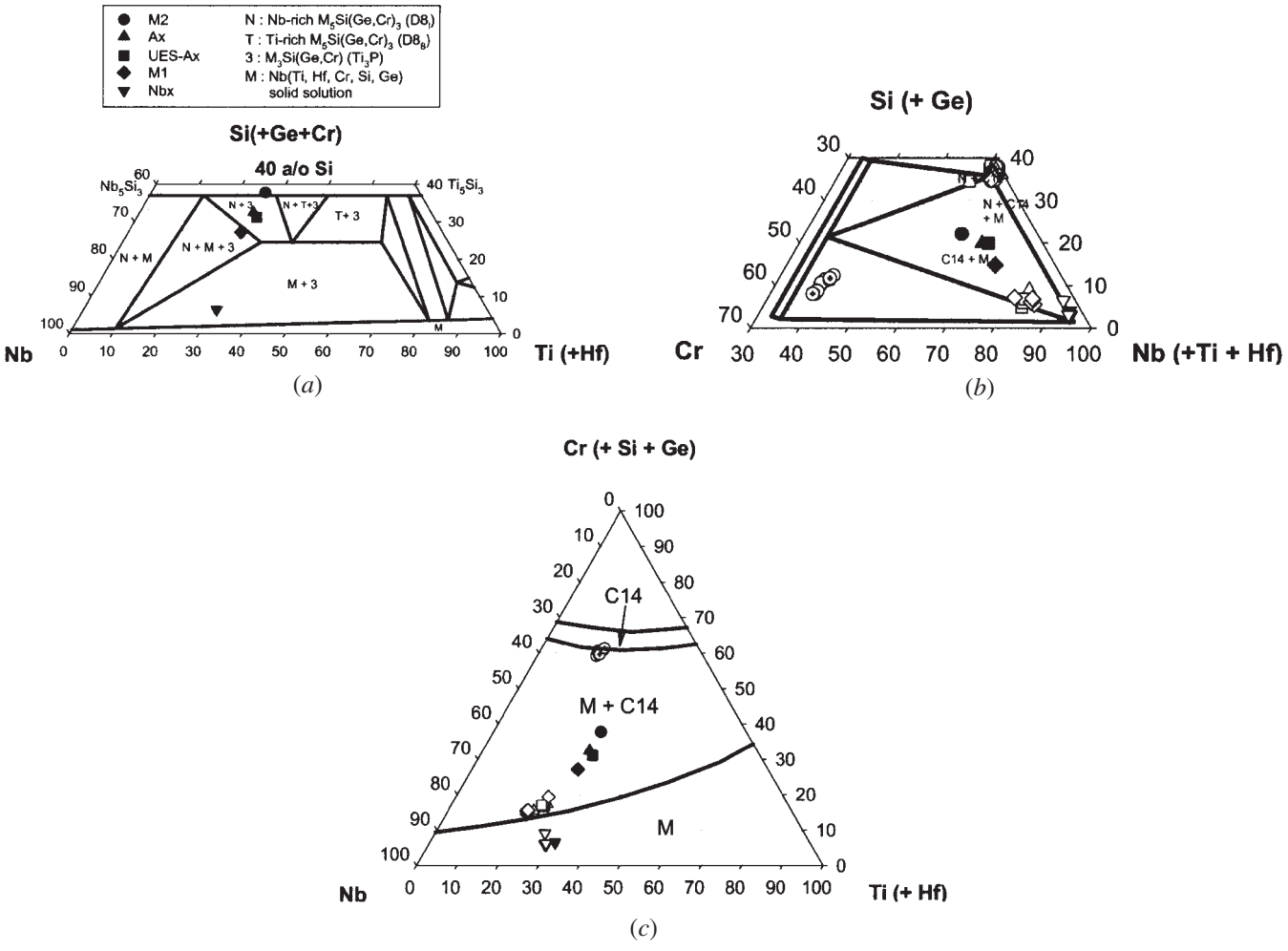

Fig. 6—Pseudoternary phase diagrams illustrate the phase relations in Nb-based *in-situ* composites at 1350 °C: (*a*) Nb-Ti(+Hf)-Si(+Ge +Cr), (*b*) Cr-Nb(+Ti + Hf)-Si(+Ge), and (*c*) Nb-Ti(+Hf)-Cr(+Si + Ge). A pseudoternary Nb-Ti-Si phase diagram is shown in *(a)*, where (+Hf) designates that Hf is added to the Ti value and (+Ge + Cr) indicates that Ge and Cr are added to the Si value. Similar conventions are used (*b*) for Cr-Nb-Si and *(c)* for Nb-Ti-Cr. Solid lines are phase boundaries from the literature.[11,12] Open symbols are compositions determined on individual phases in the *in-situ* composites. Closed symbols are nominal compositions of the composites.

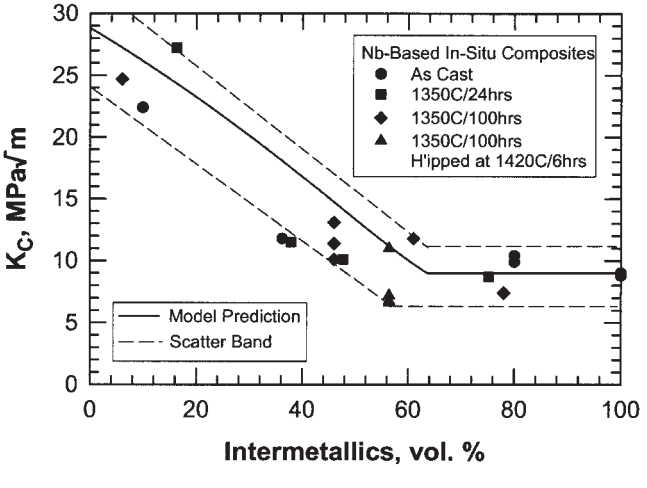

Fig. 7—Fracture toughness (K_C) decreases with increasing volume percent of intermetallics (Ge-rich phase, silicides, and Laves phases).

Fracture testing using compact-tension specimens indicated that the M2, AX, UES-AX, and CNG-1B alloys exhibited small amounts of stable crack growth and very flat K_R curves. The fracture process in as-cast M2 is summarized in the BSE images of the crack-tip region in Figures 11(a) through (d). At $K = 5$ MPa$\sqrt{\text{m}}$. microcracks formed ahead of the main crack due to cracking of the Laves phase (dark) and Ti-rich silicides (light gray), as shown in Figure 11(a). The microcracks opened up at $K = 6$ MPa$\sqrt{\text{m}}$, but did not extend. At $K = 7$ MPa$\sqrt{\text{m}}$, some of the microcracks linked up, and a new microcrack nucleated in a Nb-rich silicide grain (gray phase) located ahead of the crack tip (Figure 11(b)). At $K = 8$ MPa$\sqrt{\text{m}}$, the main crack linked up with a few microcracks, but a larger microcrack extended unstably over a distance of $\approx$290 μm (Figure 11(c)). The new crack tip at $K = 8$ MPa$\sqrt{\text{m}}$ is shown in Figure 11(d). Loading to $K = 8.5$ MPa$\sqrt{\text{m}}$ caused the main crack to extend through a few Nb-rich silicide grains. Furthermore, additional microcracks were nucleated ahead of the main crack. Most of the microcracks initiated in the Laves grains (dark), which

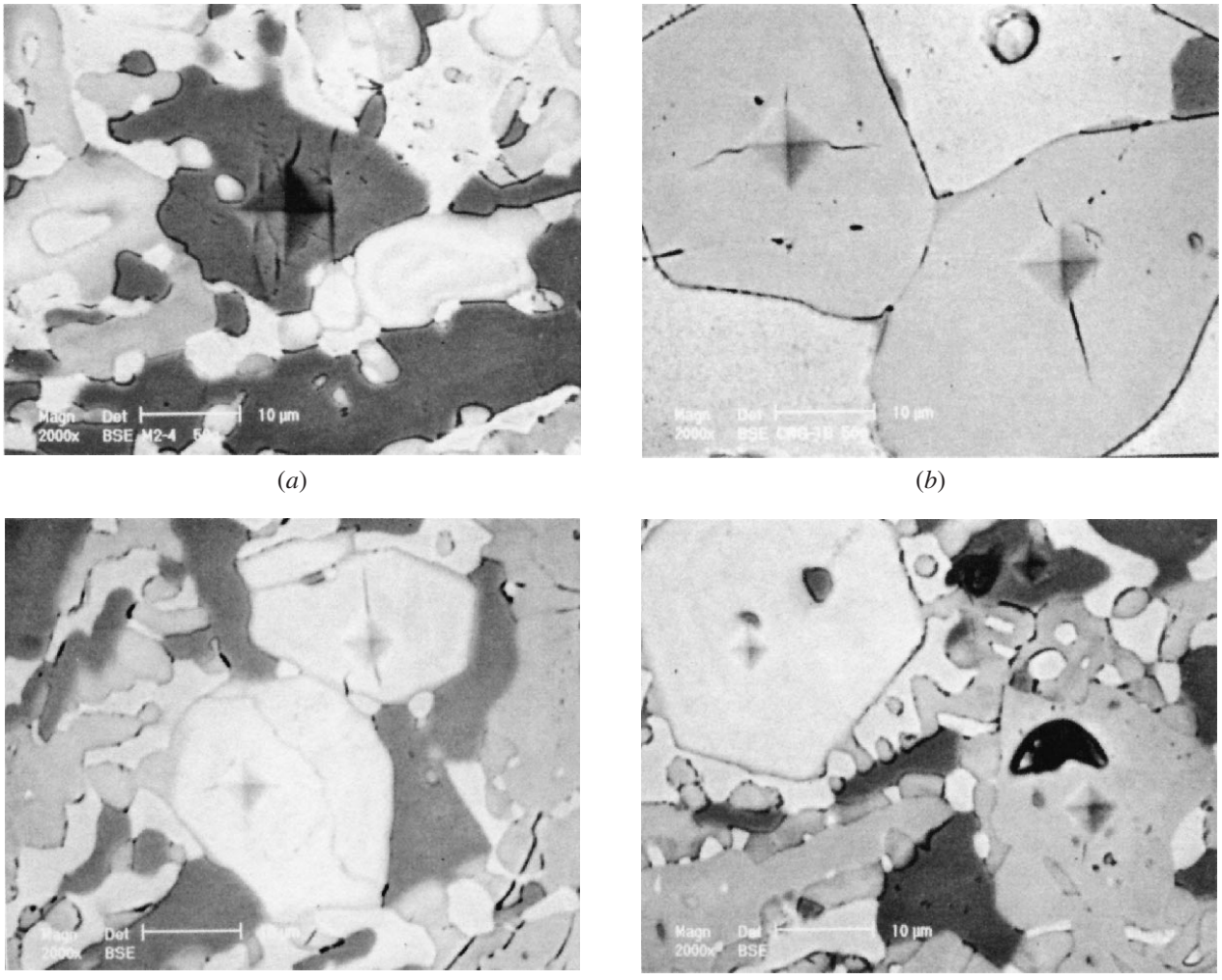

Fig. 8—Indentation cracks in constituent phases in Nb-based *in-situ* composites: (*a*) Laves phase in M2-3 (50-g load, $K = 5$ MPa$\sqrt{\text{m}}$), (*b*) silicide in CNG-1B (50-g load, $K = 7$ MPa$\sqrt{\text{m}}$), (*c*) silicide solid solution in M2-3 (25-g load, $K = 7$ and 13 MPa$\sqrt{\text{m}}$), and (*d*) Nb solid solution in Nbx-3 (25-g load, no crack, $K \geq 28$ MPa$\sqrt{\text{m}}$).

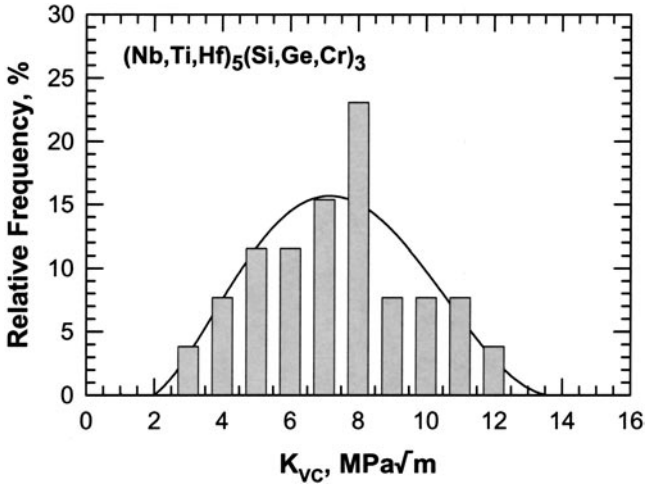

Fig. 9—Frequency distribution of the indentation fracture toughness (K_{VC}) of constituent silicide phases in Nb-based *in-situ* composites.

subsequently propagated into and arrested in Nb-rich silicides. A further increase in load led to unstable crack propagation at $K = 8.8$ MPa$\sqrt{\text{m}}$.

The fracture processes in alloys containing Nb_{ss} exhibited only small amounts of ductile-phase toughening. In as-cast AX, the main crack and microcracks were often blocked or trapped by Nb_{ss} particles, as shown in Figure 12(a) for $K = 8$ MPa$\sqrt{\text{m}}$. The main crack, however, penetrated into the Nb_{ss} particle at $K = 8$ MPa$\sqrt{\text{m}}$ (Figure 12(b)) and, subsequently, linked up with the microcrack, causing unstable fracture at $K = 9.9$ MPa$\sqrt{\text{m}}$. Crack bridging by Nb_{ss} particles was also observed in heat-treated UES-AX (1350 °C/100 hours). Figure 13(a) shows the bridged crack at $K = 7$ MPa$\sqrt{\text{m}}$. Increasing the K levels incrementally to 8 and 9 MPa$\sqrt{\text{m}}$ caused the crack to open up without lengthening. At $K = 10$ MPa$\sqrt{\text{m}}$ the main crack propagated into a Laves grain (dark) and a Nb-rich silicide grain (gray), as shown in Figure 13(b). At $K = 11$ MPa$\sqrt{\text{m}}$, the main crack propagated across several silicide and Laves grains,

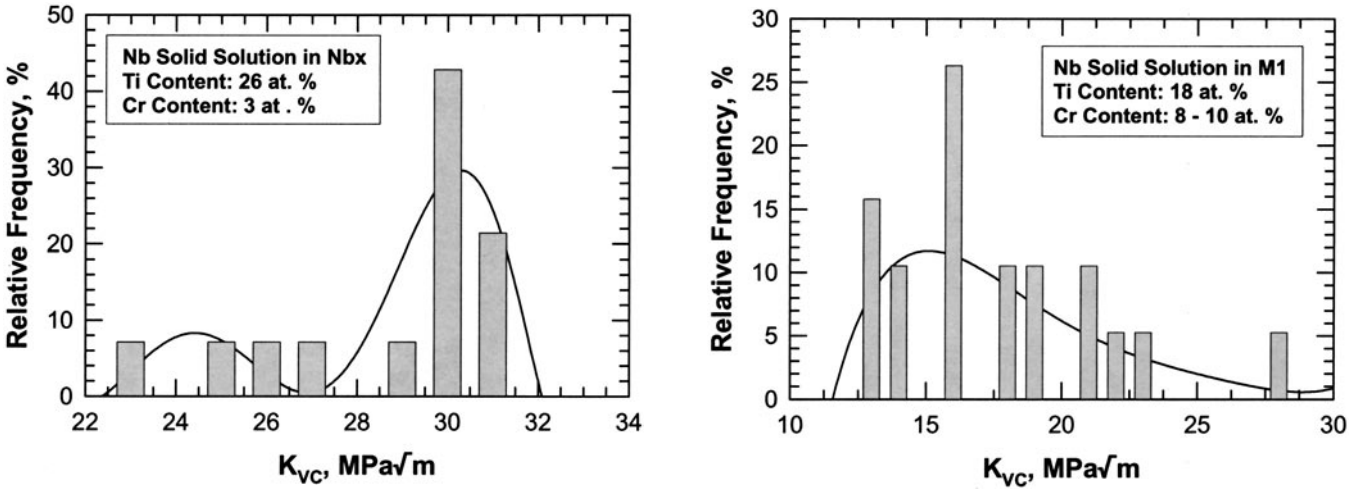

Fig. 10—Frequency distribution of the indentation fracture toughness (K_{VC}) of the Nb solid solution phase in *in-situ* composites: *(a)* high Ti and low Cr contents and *(b)* low Ti and high Cr contents.

sometimes along grain boundaries. A subsequent increase in the applied load led to unstable fracture at $K = 11.4$ MPa$\sqrt{\text{m}}$.

In CNG-1B, the crack tended to follow the silicide phase. At lower K levels, the crack was seen to arrest at or within an Nb_{ss} grain. The main crack, however, was able to get around the more ductile Nb_{ss} grains by crack reinitiation or deflection. Figure 14(a) illustrates the reinitiation of a microcrack in a silicide grain, located ahead of the trapped initial crack at $K = 6$ MPa$\sqrt{\text{m}}$. In contrast, Figure 14(b) shows that the main crack changed its path to follow the silicide phase by deflecting to propagate around the Nb_{ss} obstacles at $K = 8$ MPa$\sqrt{\text{m}}$. Consequently, the crack path follows mostly the silicide phase at $K = 9$ MPa$\sqrt{\text{m}}$. (Figure 14(c)), resulting in the absence of ductile-phase toughening and a flat K_R curve.

V. DISCUSSION

A. *Microstructure*

The characteristic diffraction peaks of Nb are close to those of the silicides (Nb_5Si_3, Nb_3Si, and Ti_5Si_3). Consequently, considerable amounts of effort were spent on the EDS of individual light phases in the BSE mode, to confirm the XRD result that the Nb_{ss} did not exist in the as-cast M2 alloy. More than 40 light and gray grains were examined, and they were all silicides. The Nb_{ss} can be easily identified by its low Si content (1 to 3 pct), while the silicides are typically rich in Si (27 to 30 pct). The Laves phases contain typically about 8 to 9 pct Si and are high in Cr (47 to 53 pct). In CNG-1B, Cr in the Laves phase is partially replaced by Fe. Thus, Cr and Fe may be considered similar, if not equivalent. Based on the XRD and EDS results, the authors are confident that the as-cast M2 contained little or no Nb_{ss} in the microstructure. Nb_{ss}, however, existed in the heat-treated materials. The volume fractions of the Laves phase are approximately the same in all alloys before and after heat treatments; thus, the Nb_{ss} formed at the expense of mostly the silicides during heat treatment at 1350 °C. Since Nb_{ss} contains 10 to 14 pct Cr and 1 to 3 pct Si, while the silicides contain 1 to 3 pct Cr and 25 to 29 pct Si, repartitioning of Cr and Si in the Nb_{ss}, silicide, and Laves phase must have occurred. The repartitioning process of these elements is not understood, but it could have involved dissolution of the Laves phase and minor changes in the volume fraction of the Laves phase. The various silicides and Laves phases and their compositions observed in the present *in-situ* composites are generally consistent with those identified by researchers at the AFRL[4,9,10] and GE Global Research Laboratories.[5,6,11,12] The C14 Laves phase is mainly the result of the stabilization of this phase by Si.[11,12] It should also be noted that Ti partitions in the Nb_{ss}, Laves phase, and silicides. The solubility of Ti in the Nb_{ss} in the *in-situ* composites appears to have a range of 18 to 26 pct, while it is about 18 to 22 pct in Nb-rich silicides but is 26 to 28 pct in Ti-rich silicides. The Cr content in the Nb_{ss} was expected to be about 3 at. pct.[11,12] This level of Cr content was observed in the Nbx alloy only. For other alloys, the Cr content in the Nb_{ss} phase was in the 9 to 14 at. pct range. Si and Ge additions appeared to increase the Cr solubility in the Nb_{ss} phase. Unfortunately, this high level of Cr significantly reduced the fracture toughness of the Nb_{ss} phase.[17,25]

B. *Alloying Effects*

The fracture toughness of Nb solid-solution alloys is known to depend on the Ti content.[17,25] A correlation between K_C and Ti content has been established in an earlier study.[25] The fracture toughness and Ti content of the Nb_{ss} phase in individual composites are compared against the experimental data and the established relation of Nb solid-solution alloys in Figure 15. The comparison indicates that there is reasonable agreement between the fracture toughness of individual Nb_{ss} particles in the *in-situ* composites and those obtained for bulk materials with equivalent Ti contents. The exception is Nbx, whose fracture tough-

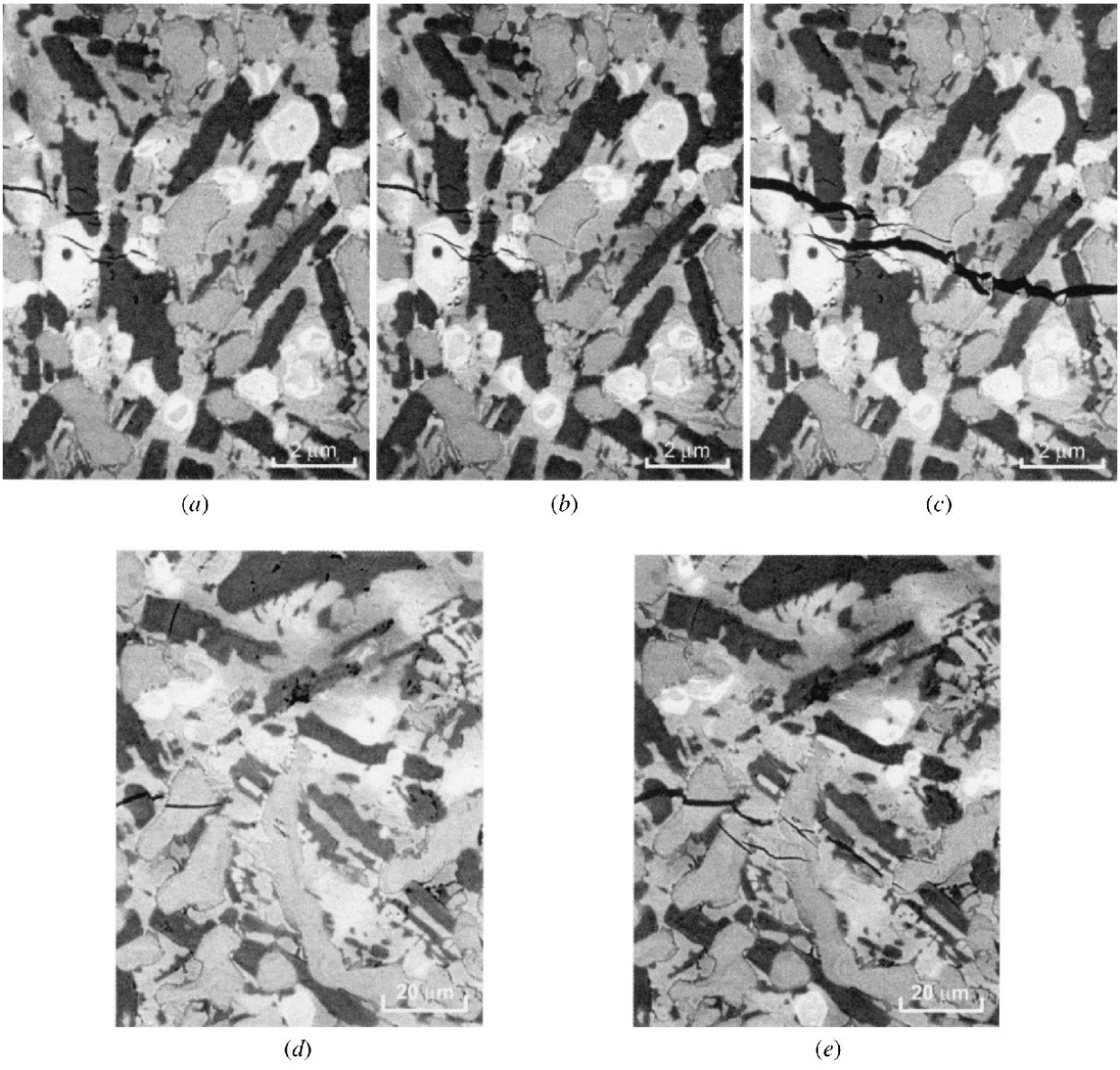

Fig. 11—Near-tip fracture processes observed in as-cast M2: (*a*) 5 MPa$\sqrt{m}$, (*b*) 7 MPa$\sqrt{m}$, (*c*) 8 MPa$\sqrt{m}$, (*d*) 8 MPa$\sqrt{m}$, new crack tip, and (*e*) 8.5 MPa$\sqrt{m}$. The light phase is $(Ti, Nb)_5Si_3$ ($D8_8$); the gray phase is $(Nb, Ti)_5Si_3$ ($D8_1$); and the dark phase is C14 Laves phase. Notch on the left; and crack growth from left to right.

ness of the Nb_{ss} phase could not be determined accurately by the indentation technique, because indentation cracks could not be induced. Because of the lack of indent cracks, the deduced fracture-toughness values for the Nb_{ss} phase Nbx are minimum values, and they are not shown in Figure 15. The experimental data are compared against the empirical fit (dashed line) developed earlier,[25] as well as against computed values based on a thermally activated slip model. For elastic-plastic fracture,

$$J_c = J_s + J_p \qquad [2]$$

where J_s and J_p, the J integrals contributed by elastic and plastic processes during fracture, respectively, are given by[17]

$$J_s = 2\gamma_s \qquad [3]$$

and

$$J_p = J_0 \exp\left(- \frac{U_{P-N} b^2}{kT} \right) \qquad [4]$$

where J_0 is a constant at a constant T and $J_0 = 5 \times 10^4$ J/m^2 for 298 K; b is the magnitude of the Burgers vector; U_{P-N} is the Peierls-Nabarro barrier energy; k is Boltzmann's constant; and T is the absolute temperature. Equations [3] and [4] can be summed to give Eq. [2], leading to

$$K_c = \sqrt{\frac{E(J_s + J_p)}{(1 - \nu^2)}} \qquad [5]$$

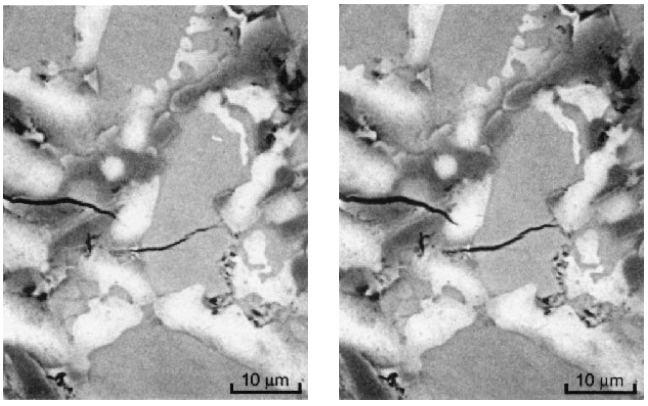

(*a*) (*b*)

Fig. 12—Crack-tip interactions with Nb_{ss} particles in as-cast AX: (*a*) crack-tip trapping by Nb_{ss} at $K = 8$ MPa$\sqrt{m}$, and (*b*) crack-tip penetration into an Nb_{ss} particle at $K = 9$ MPa$\sqrt{m}$ The light phase is Nb_{ss}; the gray phase is $(Nb, Ti)_5Si_3$ ($D8_1$); and the dark phase is C14 Laves phase.

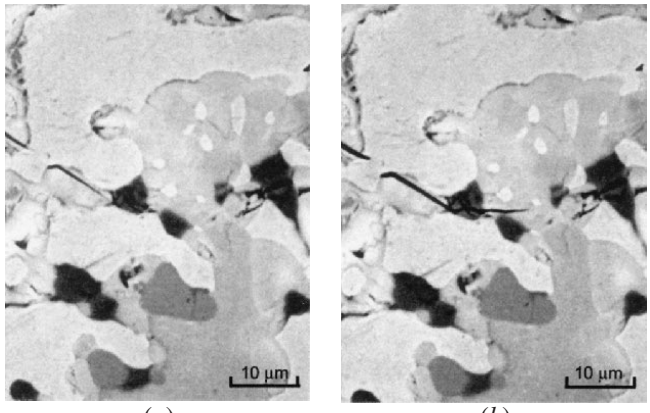

(*a*) (*b*)

Fig. 13—Crack bridging by Nb_{ss} particles in heat-treated UES-AX (1350 °C/100 h): (*a*) bridged crack at $K = 7$ MPa$\sqrt{m}$, and (*b*) crack extension into Laves and Nb_{ss} grains as K increased to 10 MPa$\sqrt{m}$. The light phase is Nb_{ss}; the gray phase is silicide; and the dark phase is C14 Laves phase.

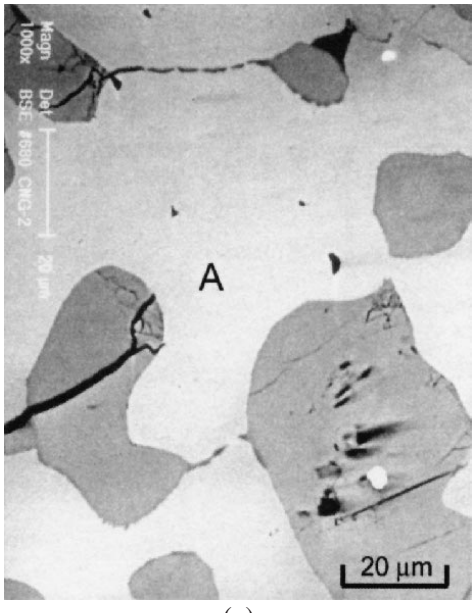

(*a*)

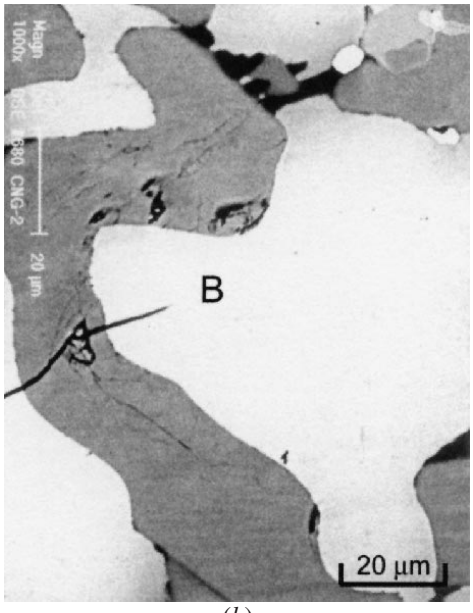

(*b*)

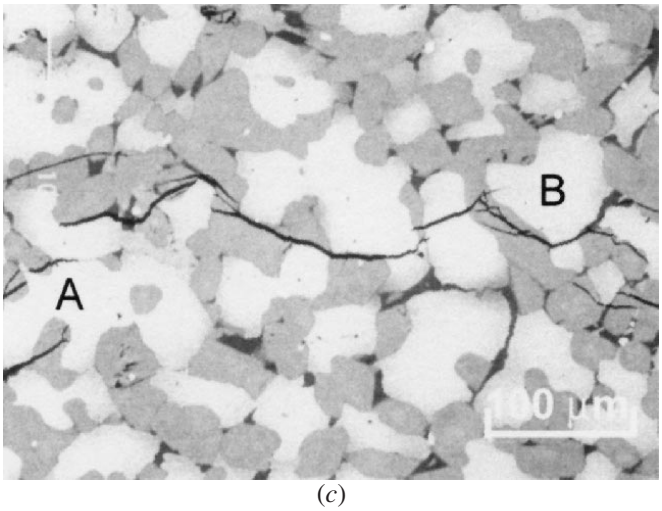

(*c*)

Fig. 14—The crack path follows mostly the silicide phase in the CNG-1B alloy: (*a*) crack reinitiation in a silicide when the main crack is trapped by an Nb_{ss} grain at $K = 6$ MPa$\sqrt{m}$, (*b*) crack deflection around an Nb_{ss} grain and into silicide phase at $K = 8$ MPa$\sqrt{m}$, and (*c*) microscopic view of the crack path at $K = 9$ MPa$\sqrt{m}$. Notch on the left. Crack growth from left to right. The light phase is Nb_{ss}, the gray phase is silicide, and the dark phase is Laves phase.

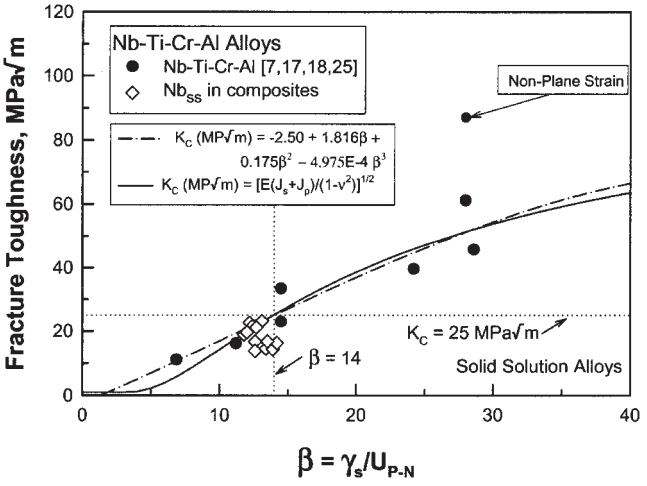

Fig. 15—Fracture toughness (K_C) of Nb solid solution alloys as a phase in composites and as a function of the ratio of surface energy, γ_s, to the P–N barrier energy, U_{P-N}. Empirical fit was from Chan.[25]

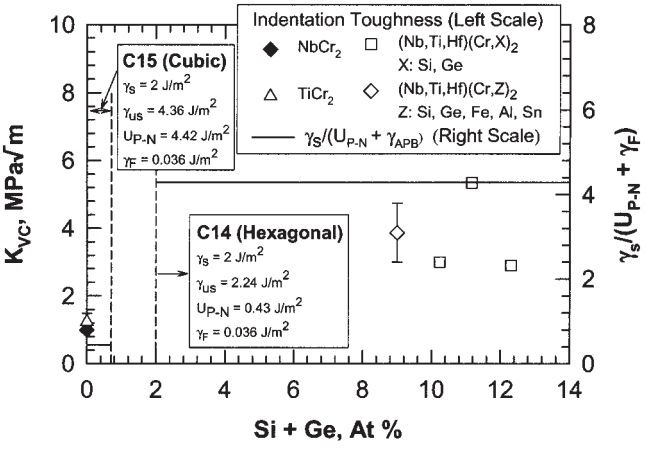

Fig. 16—Fracture toughness, unstable stacking energy (γ_{us}), P–N barrier energy (U_{P-N}), and crystal structure of Laves phase as a function of Si and Ge addition.

for plane-strain fracture in isotropic materials with a Young's modulus, (E) and Poisson's ratio, (ν). The solid line in Figure 15 shows the computed K_c as a function of γ_s/U_{P-N} for Nb_{ss} using Eq. [3] through [5] and $\gamma_s = 2$ J/m^2, $J_0 = 5 \times 10^4$ J/m^2 and $b^2/kT = 20$ Since $\gamma_s \cong$ constant, K_C varies with U_{P-N}; thus, the dependence of K_C can be rationalized and treated as a manifestation of thermally activated slip.

$NbCr_2$ has a C15 (cubic) crystal structure and a fracture toughness of about 1 MPa$\sqrt{m}$ at ambient temperature.[7,8,20] As shown in Figure 16, a small (>2 at. pct) addition of Si+ Ge changes C15 $NbCr_2$ to C14 (hexagonal), which is normally stable only at elevated temperatures. In addition, the Si and Ge addition improves the fracture toughness of $NbCr_2$ from 1 MPa$\sqrt{m}$[7,8,20] to about 2 to 5 MPa$\sqrt{m}$. Computations of unstable stacking energy and P–N barrier energy were performed for deformation of C15 by synchroshear[50] of a pair of 1/6 $<\bar{2}11>$ partial dislocations on a {111} plane in C15 and C14.[51] These results indicated that $\gamma_{us} = 4.36$ J/m^2 and $U_{P-N} = 4.42$ for synchroshear in C15.[51] In contrast, $\gamma_{us} = 2.24$ J/m^2 and $U_{P-N} = 0.43$ J/m^2 for {0001}1/3 $<10\bar{1}0>$ synchroshear in C14, because of a more favorable ratio of the slip-plane separation to the Burgers vector (d/b). The lower values of γ_{us} and U_{P-N} suggest that dislocation glide or twinning by synchroshear may be easier in the C14 than in the C15 Laves phase. Consequently, a Si or Ge addition to $NbCr_2$ should improve the fracture resistance when C14 phase is stabilized, as observed experimentally.

Nb_5Si_3 can exist in either the $D8_m$ or $D8_1$ crystal structures; both are bct phases whose deformation mechanisms are still unknown. On the other hand, Ito *et al.*[52] identified <100>{012},<100>(001), 1/2<111>{110}, and <110>(001) as possible slip systems in Mo_5SiB_2 (T2 phase, $D8_1$ structure). Experimental evidence, however, indicates that [001](010) is the operative slip system in the T2 phase at 1500 °C.[52] Because of the complex $D8_1$ structure, slip in T2 appears to occur through the actions of three fractional [001] partial dislocations separated by two complex stacking faults (CSFs), according to the dissociation reaction given by[52]

$$[001] \rightarrow 0.26[001] + CSF + 0.48[001] + CSF + 0.26[001] \quad [6]$$

which was suggested by Ito *et al.*,[52] through a consideration of the overlapping volume encountered by atoms on the slip plane. Taking Eq. [6] as the operative slip mechanism, theoretical calculation indicates that the dislocation dissociation reaction is energetically favorable, and it leads to a significant reduction in both the unstable stacking and P–N barrier energies in Nb_5Si_3 with the $D8_1$ crystal structure. Recent computations indicated that the γ_{us} and U_{P-N} values for [001](010) slip in Nb_5Si_3 are 8.88 and 9.81 J/m^2, respectively.[51] In contrast, the γ_{us} and U_{P-N} values are reduced to 3.25 and 0.01 J/m^2, respectively, if slip on (010) is accomplished by three fractional [001] partial dislocations. An alloying addition that promotes slip by the fractional [001] partial dislocations should improve the fracture resistance of Nb_5Si_3.

The fracture toughness of Nb_5Si_3 has been found to improve with the additions of Ti. In particular, the fracture toughness of alloyed $(Nb,Ti,Hf)_5(Si,Cr,Ge)_3$ silicide appears to increase with increasing Ti additions but decrease with the bond order, as shown in Figure 17(a). Bond order is a measure of the strength of the covalent bond between atoms and is computed on the basis of the overlapping electron population.[53] This enhancement of fracture resistance by a Ti addition and its relation to bond order is not well understood. One possible explanation is that the Ti addition promotes the slip by the partial dislocation mechanism, as described in Eq. [6]. Previously, Ito *et al.*[52] suggested that the driving force for dislocation dissociation is the need to minimize the overlapping volume of atoms on the slip plane. Ito *et al.*[52] demonstrated this point in terms of contours of overlapping volume derived on the basis of a hard-ball model that was used to represent the atomic interference on the slip plane. Since the Ti addition reduces the bond order of Nb_5Si_3, the overlapping electron population and, possibly, the overlapping volume are reduced by Ti additions. Such a reduction of the overlapping volume, if proven to occur, could promote the

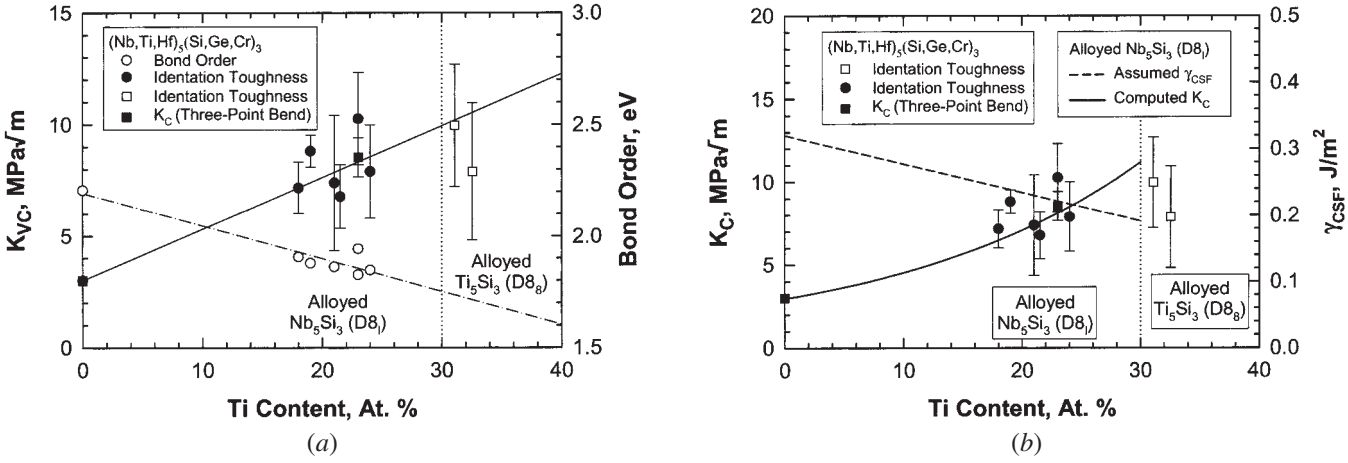

Fig. 17—(*a*) Fracture toughness (left side) and bond order (right side) of alloyed silicides as a function of Ti content. Trend lines are shown, and (*b*) computed K_C compared against experimental data and the complex stacking fault energy, γ_{CSF}, required to fit the fracture model to the experimental data of alloyed Nb_5Si_3.

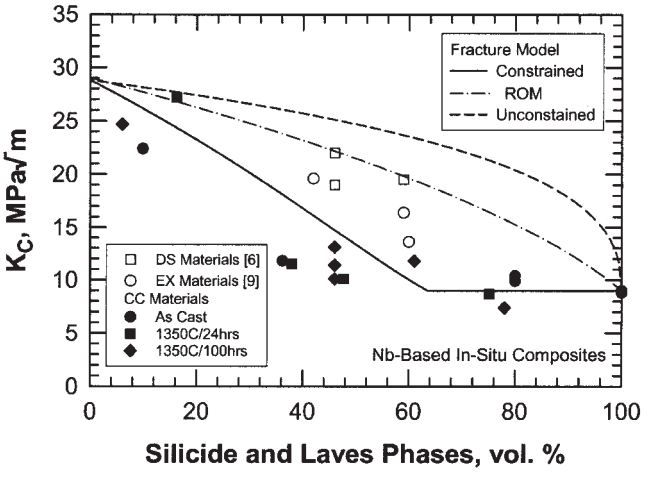

Fig. 18—A comparison of the fracture toughness values of conventionally cast (CC), directionally cast (DS), and extruded (EX) Nb-based *in-situ* composites against model calculations based on crack-tip trapping/bridging with and without plastic constraint, and the rule of mixtures (ROM).

partial-slip process by reducing the unstable stacking energy, the CSF energy, or the P–N barrier energy.

The beneficial effect of a reduced CSF energy on the fracture toughness of the $(Nb,Ti)_5Si_3$ silicides ($D8_1$) was evaluated by fitting Eq. [4] to the fracture-toughness data by adjusting the CSF energy. The computed K_C and the deduced CSF energy are shown in Figure 17(b). The computation indicated that the CSF energy required to give the observed fracture toughness is in the range of 0.2 to 0.3 J/m^2, which is substantially lower than the 0.89 J/m^2 value for the CSFs observed in Mo_5SiB_2. This reduction of the CSF energy, if proven to occur, would explain the increase of fracture resistance exhibited by Nb_3Si_3 alloyed with Ti additions. Obviously, high-resolution transmission electron microscope studies of the dislocation structure and a determination of the CSF energy in alloyed Nb_5Si_3 are required to verify this hypothesis. The effects of a Ti addition on the lattice parameter, the *d* spacing of the possible (or most likely) slip planes, and b may be determined by XRD, but the necessary analyses of the XRD data have not been performed.

The preceding sections illustrate the importance of compositional design on the fracture resistance of individual phases in the *in-situ* composites. Alloy composition alone, however, is not sufficient to ensure high fracture toughness. The size, shape, and morphology of individual phases are also important factors influencing the fracture resistance of Nb-based *in-situ* composites. Figure 18 shows a comparison of the K_C values of conventionally cast (CC), directionally cast (DS),[6] and extruded (EX) Nb-based *in-situ* composites.[3,9] The DS and EX materials exhibit a higher fracture toughness than the CC materials.

The fracture mechanism in the in-situ composites involves the formation of microcracks ahead of the main crack. Most of these microcracks are initiated in the Laves phase, which has the lowest fracture toughness among the constituent phases in the microstructure. Once initiated in the Laves phase, the microcracks propagate into the silicide phase. The linkage of the main crack and microcracks, which dictates the observed fracture toughness, often occurs without plastic stretching of the Nb_{ss} particles. The absence of ductile-phase toughening in the Nb-based in-situ composites appears to originate from the phase morphology in the composite microstructure. In-situ fracture-toughness testing results, shown in Figure 11 through 14, revealed that the lower fracture toughness exhibited by the CC materials was the consequence of a relatively continuous silicide phase in the microstructure, such that the crack path resided in the silicide and Laves phases. Because of this fracture path, the ductile Nb solid solution was not able to enhance the fracture toughness of the in-situ composites. Comparison of the experimental data against the theoretical calculation of a fracture-toughness model[32] suggested that the lack of ductile-phase toughening by the Nb solid-solution phase was caused by the high plastic constraint induced by the continuous matrix of silicide and Laves phases. In particular, Figure 18 shows the computed K_c curves for crack-tip trapping/bridging[54] by ductile phase in the in-situ composites with (solid curve) and without (dashed curve) plastic constraint acting on the Nb_{ss} phase, as well as that computed based on the rule of mixtures (ROM). The K_c curve without plastic constraint and that for the ROM were computed using Eqs. [4] and [12] of Chan and Davidson,[32] respectively, while the K_c curve with

the plastic constraint (solid curve) was computed using Eqs. [10] and [11] of Chan and Davidson.[32] For these calculations, $q = 1$ and $K_d = 28\ \text{MPa}\sqrt{\text{m}}$ as the average value of the fracture toughness of Nb_{ss}. For spherical particles, the intermetallics begin to make contact when their volume percents exceed the theoretical value of ≈ 72 pct and the crack can propagate exclusively in the intermetallic phase. For irregular-shaped particles, the intermetallic phase can occur with high contiguity at a lower volume fraction. This appears to be case in the Nb-based in-situ composites. The fracture toughness of the in-situ composites was essentially identical to that of the silicides when the volume fraction of intermetallics was greater than approximately 60 pct (Figures 7 and 18). At the present time, it is unclear why the DS and EX materials exhibited a higher fracture toughness than the CC materials, but it appears to originate from the lack of contiguity of the intermetallic and the changes in plastic constraint associated with the shape of the Nb_{ss} in the DS and EX microstructures.

C. *Computational Design*

The observed fracture-toughness values of the *in-situ* composites are not as high as those predicted by the computational design model. The discrepancy can be attributed to several sources. First, the sum of Ti and Hf contents in the Nb_{ss} phase apparently has an upper limit, as none was able to exceed 29 pct in the presence of Nb-rich and Ti-rich silicides. In contrast, the Cr content increased to 10 to 14 pct. Previous work has shown that the fracture resistance of Nb_{ss} increases with increasing Ti additions,[17,25] but decreases with increasing Cr additions;[17,25] both have combined in the present composites to limit the fracture toughness of the Nb_{ss} phase. Second, the volume fraction of intermetallics is somewhat higher than that expected and assumed in the model. Since the design calculations were based on alloys without Ge, the addition of Ge to the composites appears to have altered the phase boundaries and the phase relations. Third, the silicide phase exhibits a high degree of contiguity, and a continuous path exists in the silicide phase for the crack to follow. As a result, the crack bypassed the more ductile Nb_{ss} and resulted in a composite toughness that corresponds to the fracture toughness of the silicide phase (8 to $10\ \text{MPa}\sqrt{\text{m}}$). Fourth, the Laves phase appears to serve as an initiation site where microcracks nucleate (by virtue of its lower fracture toughness) and then propagate into the silicide phase. Finally, a high plastic constraint exists in the Nb_{ss} that has prevented ductile-phase toughening from fully developing in the *in-situ* composites with a high intermetallic content. The high plastic constraints were not relaxed by the heat treatments used in this study. It is thought that all of these factors contribute to limit the fracture resistance of the *in-situ* composites and have caused the discrepancy between the experimental results and the model prediction for the unconstrained case.

To improve the fracture resistance of the *in-situ* composites, the volume fraction of the Laves phase should be reduced because of its low fracture toughness, providing that the oxidation resistance is not reduced. Similarly, the Ge addition should be reduced, since it tends to induce the formation of second phases along grain boundaries. More importantly, the microstructural constraint on the Nb_{ss} needs to be reduced either by modifying the size and morphology of the constituent phases or their interface properties. The required microstructural modifications include (1) relatively large and elongated Nb_{ss} grains and (2) submicron or nanosized shearable silicide particles that are coherent with Nb_{ss}. *In-situ* composites with elongated Nb_{ss} particles have been achieved by extrusion[9] or directional solidification,[6] and improvements in fracture toughness have been made. Previous attempts were successful in reducing the size of Laves phase to the 1 to 2 μm range by rapid solidification[55] and mechanical alloying[56] techniques. To refine the silicides to the nanoscale range may be a difficult task. Alternately, the alloying addition may be used to reduce the interface energy between the Nb_{ss} and silicides, in order to facilitate emission of dislocations from the interface or crack penetration into the Nb_{ss} particles.

The computational design method was successful in the sense that its predictions were realized in most cases. In particular, the computational model predicted correctly the effects of alloy additions (Ti, Cr, Hf, Al, *etc.*) and the volume fractions of intermetallics on the fracture resistance of the Nb_{ss} phase and the *in-situ* composites, respectively. As discussed in more detail in a separate article,[34] the computational model predicted correctly that the oxidation resistance of the Nb_{ss} and the *in-situ* composites would not come from the formation of SiO_2, but would depend on the Cr content, since Cr-based oxides are likely to form instead of SiO_2 (Figure 1(b)). However, the computational model was not successful in improving or optimizing the fracture and oxidation resistance at the same time, because of the opposite effects of Ti and Cr additions on constituent properties and the different roles of constituent phases in the composite properties. For example, Ti improves the fracture resistance but reduces the oxidation resistance, while a Cr addition produces the opposite effects. Similarly, a large volume fraction of Nb_{ss} improves the fracture resistance but reduces the oxidation resistance, and *vice versa* for a large volume fraction of intermetallics. Because of this, the fracture and oxidation resistance of the *in-situ* composites could not be optimized to meet the property goals for the same microstructure. To overcome these difficulties, a microstructure with fine shearable particles is needed, so that the constraint on Nb_{ss} could be relaxed even at high intermetallic contents and SiO_2 could be induced to form beneath the Cr oxide layers.

VI. CONCLUSIONS

A computational method was used to design the composition and microstructure of several *in-situ* composites based on the Nb-Ti-Hf-Cr-Si-Ge system, with the objective of achieving balanced properties of creep, oxidation, and fracture resistance. The candidate materials were fabricated and evaluated. This article described the evaluation of the fracture toughness of the constituent phases and the composites of the candidate alloys. The conclusions reached in this study are as follows.

1. An addition of Si and Ge in $NbCr_2$ stabilized the C14 and increased the fracture toughness from 1 to 2 to $5\ \text{MPa}\sqrt{\text{m}}$. The toughness enhancement may be attributed to a reduction of unstable stacking and P-N barrier energies for slip by synchroshear in the C14 structure.

2. Ti and Hf additions appeared to enhance the fracture toughness of Nb-rich and Ti-rich M_5Si_3 from 2 to 3 to 8 to 10 MPa$\sqrt{m}$. The toughness enhancement may be attributed to slip by [001] partial dislocations and correlates with increasing fracture toughness with decreasing bond order by increasing Ti and Hf additions.
3. The fracture toughness of the Nb_{ss} in the *in-situ* composites is limited to 25 to 30 MPa$\sqrt{m}$, because the Ti + Hf content is limited to 29 pct and the Cr content can reach as high as 14 pct.
4. The Cr content (10 to 14 at. pct) in the Nb solid-solution phase in the Nb-Ti-Hf-Cr-Si-Ge *in-situ* composites is higher than that ($\approx$3 at. pct) expected based on the ternary Nb-Si-Cr phase diagram.
5. A high Cr content (10 to 14 at. pct) and a high plastic constraint in the Nb solid-solution phase is responsible for the relatively low fracture resistance exhibited by the Nb-based *in-situ* composites.
6. The fracture mechanism in Nb-based *in-situ* composites containing a large volume fraction of intermetallics involves the nucleation of microcracks in the Laves phase, propagation of microcracks in the silicide phases, and linkage of the main crack with microcracks without substantial plastic stretching occurring in the Nb_{ss} particles.
7. The fracture toughness of the *in-situ* composites decreases with increasing volume fractions of intermetallics phases. Ductile-phase toughening is ineffective in composites containing more than 40 to 50 pct intermetallics, because the crack tends to propagate in the intermetallic phases and bypass the Nb_{ss} phase.
8. The fracture toughness of the Nb-based *in-situ* composites is approximately the fracture toughness of the silicide phase when the volume percent of intermetallics exceeds 60 pct.
9. The Vickers indentation technique appears to be a viable tool for characterizing the fracture toughness of the Laves and silicide phases in the Nb-based *in-situ* composites. However, a calibration curve must be developed since the induced tensile stresses acting on the indentation cracks depend on the amounts of inelastic deformation under the indentor.
10. The computational modeling effort was successful in that the predictions of the model with regard to the overall fracture and oxidation properties were essentially realized.

ACKNOWLEDGMENTS

This work was supported by the Air Force Office of Scientific Research through Contract No. F4962001-C-0016, Dr. Craig S. Hartley, Program Manager. The authors are thankful to Drs. Melvin Jackson and J.C. Zhao, General Electric Global Research Laboratories (Schenectady, NY), for supplying alloy compositions and previously unpublished phase diagrams, and to Dr. Young-Wom Kim, UES (Dayton, OH), for supplying the UES-AX and CNG-1B materials. The technical assistance of F. Campbell, J. Spencer, and B. Chapa, and the clerical assistance of Ms. L. Salas and Ms. P. Soriano, all of Southwest Research Institute, is appreciated.

REFERENCES

1. D.L. Anton and D.M. Shah: *MRS Symp. Proc*., 1990, vol. 194, pp. 175-82.
2. R.M. Nekkanti and D.M. Dimiduk: *MRS Symp. Proc*., 1990, vol. 194, pp. 175-82.
3. M.G. Mendiratta and D.M. Dimiduk: *Metall. Trans. A*, 1993, vol. 24A, pp. 501-04.
4. P.R. Subramanian, M.G. Mendiratta, and D.M. Dimiduk: *JOM*, 1996, vol. 48, pp. 33-38.
5. M.R. Jackson, B.P. Bewlay, R.G. Rowe, D.W. Skelly, and H.A. Lipsitt: *JOM*, 1996, vol. 48, pp. 39-44.
6. B.P. Bewlay, M.R. Jackson, and H.A. Lipsitt: *Metall. Mater. Trans. A*, 1996, vol. 27A, pp. 3801-08.
7. D.L. Davidson, K.S. Chan, and D.L. Anton: *Metall. Mater. Trans. A*, 1996, vol. 27A, pp. 3007-18.
8. K.S. Chan and D.L. Davidson: *JOM*, 1996, vol. 48(9), pp. 62-68.
9. P.R. Subramanian, M.G. Mendiratta, D.M. Dimiduk, and M.A. Stucke: *Mater. Sci. Eng*., 1997, vols. A239–A240, pp. 1-13.
10. H.A. Lipsitt, M. Blackburn, and D.M. Dimiduk: in *Intermetallic Compounds—Principles and Practice—Vol*. 3, J. H. Westbrook and R.L. Fleischer, eds., John Wiley, New York, NY, 2002, pp. 471-99.
11. B.P. Bewlay and M.R. Jackson: in *Comprehensive Composite Materials*, A Kelly and C. Zweben, eds. vol. 3, *Metal Matrix Composites*, T.W. Clyne, ed., Elsevier, New York, NY, 2000, vol. 3, pp. 579-613.
12. J.-C. Zhao, B.P. Bewlay, M.R. Jackson, and L.A. Peluso: in *Structural Intermetallics 2001*, K.J. Hemker, D.M. Dimiduk, H. Clemens, R. Darolia, H. Inui, J.M. Larsen, V.K. Sikka, M. Thomas, and J.D. Whittenberger, eds. TMS, Warrendale, PA, 2001, pp. 483-91; also J.-C. Zhao: GE CR&D, Schenectady, NY, private communication, 2001.
13. P.R. Subramanian, M.G. Mendiratta, and D.M. Dimiduk: *MRS Symp. Proc*., 1994, vol. 322, pp. 491-502.
14. B.P. Bewlay, M.R. Jackson, W.J. Reeder, and H.A. Lipsitt: *MRS Symp. Proc*., 1995, vol. 364, pp. 943-48.
15. J.D. Rigney, P.M. Singh, and J.J. Lewandowski: *JOM*, 1992, vol. 44(8), pp. 36-41.
16. J. Kajuch, J. Short, and J.J. Lewandowski: *Acta Metall. Mater*., 1995, vol. 43, pp. 1955-67.
17. K.S. Chan and D.L. Davidson: *Metall. Mater. Trans. A*, 1999, vol. 30A, pp. 925-39.
18. D.L. Davidson and K.S. Chan: *Metall. Mater. Trans. A*, 1999, vol. 30A, pp. 2007-18.
19. K.S. Chan: *Mater. Sci. Eng*., 2002, vols. A329–A331, pp. 513-22.
20. D.J. Thomas, K.A. Nibur, K.C. Chen, J.C. Cooley, L.B. Dauelsberg, W.L. Hults, and P.G. Kotula: *Mater. Sci. Eng*., 2002, vols. A329–A331, pp. 408-15.
21. D. Farkas, S.J. Zhou, C. Vacilhe, B. Mutasa, and J. Panova: *J. Mater. Res*., 1977, vol. 12, pp. 93-99.
22. D. Farkas: *Mater. Sci. Eng*., 1998, vol. A249, pp. 249-58.
23. U.V. Waghmare, E. Kaxiras, V.V. Bulatov, and M.S. Duesberry: *Modelling Simul. Mater. Sci. Eng*., 1998, vol. 6, pp. 493-506.
24. J.R. Rice: *J. Mech. Phys. Solids*, 1992, vol. 40, pp. 239-71.
25. K.S. Chan: *Metall. Mater. Trans. A*, 2001, vol. 32A pp. 2475-87.
26. K.S. Chan: *Mechanisms and Mechanics of Fracture: The John F. Knott Symp*. W.O. Soboyejo, J.J. Lewandowski, and R.O. Ritchie, eds., TMS, Warrendale, PA, 2002, pp. 143-48.
27. P.B. Hirsch and S.G. Roberts: *Phil. Mag. A*, 1991, vol. 64, pp. 55-80.
28. S.G. Roberts and A.S. Booth: *Acta Mater*., 1997, vol. 45, pp. 1045-53.
29. P.B. Hirsch and S.G. Roberts: in *Cleavage Fracture, Proc. George R. Irwin Symp*., Kwai S. Chan, ed., TMS, Warrendale, PA, 1997, pp. 137-45.
30. R.E. Peierls: *Proc. Phys. Soc*., 1940, vol. 52, pp. 34-37.
31. F.R.N. Nabarro: *Proc. Phys. Soc*., 1947, vol. 59, pp. 236-394.
32. K.S. Chan and D.L. Davidson: *Metall. Mater. Trans. A*, 2001, vol. 32A, pp. 2717-27.
33. K.S. Chan: *Mater. Sci. Eng*., 2002, vol. A337, pp. 59-66.
34. K.S. Chan: Southwest Research Institute, San Antonio, TX, unpublished research, 2003.
35. M.R. Jackson: General Electric Global Research Laboratories, Schenectady, NY, unpublished research and private communications, 1999.
36. J.N. Wang: *Mater. Sci. Eng. A*, 1996, vol. A206, pp. 259-69.
37. J.N. Wang: *Acta Mater*., 1996, vol. 44, pp. 1541-46.

38. G. Wang, B. Gleeson, and D.L. Douglass: *Oxid. Met*., 1991, vol. 35, pp. 333-48.
39. Y.-W. Kim: UES, Inc., Dayton, OH, unpublished research and private communications, 2000.
40. *Annual Book of ASTM Standards*, Vol. 03.01, ASTM E39–90, ASTM, Philadelphia, PA, 1995, pp. 412-42.
41. D.L. Davidson and A. Nagy: *J. Phys. E*, 1978, vol. 11, pp. 207-10.
42. G.R. Anstis, P. Chantikul, B.R. Lawn, and D.B. Marshall: *J. Am. Ceram. Soc*., 1981, vol. 64, pp. 533-38.
43. P. Chantikul, G.R. Anstis, B.R. Lawn, and D.B. Marshall: *J. Am. Ceram. Soc*., 1981, vol. 64, pp. 539-43.
44. B.R. Lawn, A.G. Evans, and D.B. Marshall: *J. Am. Ceram. Soc*., 1980, vol. 63, pp. 574-81.
45. S. Suresh: *Fatigue of Materials*, Cambridge University Press, Cambridge, U. K. 1991, pp. 283-87.
46. J.R. Brockenbrough and S. Suresh: *J. Mech. Phys. Solids*, 1987, vol. 35, pp. 721-42.
47. S. Suresh: in *Modeling of Plastic Deformation and Its Engineering Applications*, 13th Risø Int. Symp. on Materials Science, S.I. Andersen, J.B. Bilde-Sørensen, N. Hansen, D. Juul Jensen, T. Leffers, H. Lilholt, T. Lorentzen, O.B. Pedersen, and B. Ralph, eds., Risø National Laboratory, Roskilde, Denmark, 1992, pp. 111-24.
48. Joint Committee on Powder Diffraction Files, International Center for Diffraction Data, Swarthmore, PA, 1992.
49. M.G. Mendiratta: UES, Dayton, OH, private communication, 2001.
50. P.M. Hazzledine, K.S. Kumar, D.B. Miracle, and A.G. Jackson: *MRS Symp. Proc*., 1993, vol. 288, pp. 591-96.
51. K.S. Chan: *Proc. Thermec 2003, Mater. Science Forum*, 2003, in press; also Southwest Research Institute, San Antonio, TX, unpublished results, 2003.
52. K. Ito, K. Ihara, K. Tanaka, M. Fujikura, and M. Yamaguchi: *Intermetallics*, 2001, vol. 9, pp. 591-602.
53. Y. Harada, M. Morinaga, J.I. Saito, and Y. Takagi: *J. Phys: Condens. Matter*., 1997, vol. 9, pp. 8011-30.
54. A.F. Bower and M. Ortiz: *J. Mech. Phys. Solids*, 1991, vol. 39, pp. 815-58.
55. K.S. Chan, D.L. Davidson, and D.L. Anton: *Metall. Mater. Trans. A*, 1997, vol. 28A, pp. 1797-808.
56. D.L. Davidson and K.S. Chan: *Metall. Mater. Trans. A*, 2002, vol. 33A, pp. 401-16.